Supporting Information

Chain-length dependent organisation in mixtures of hydrogenous and fluorous ionic liquids

Naomi S. Elstone,[a] Emily V. Shaw,[a] Karina Shimizu*,[b] Joshua Lai,[a] Bruno Demé,[c] Paul D. Lane,[d] Matthew L. Costen,[d] Kenneth G. McKendrick,[d] Sarah Youngs,[e] Sarah E. Rogers,[e] Jose N. Canongia Lopes,[b] Duncan W. Bruce*[a] and John M. Slattery*[a]

[a] Department of Chemistry, University of York, Heslington, York YO10 5DD, UK.
[b] Centro de Química Estrutural, Institute of Molecular Sciences, Instituto Superior Técnico, Universidade de Lisboa, Av. Rovisco Pais 1049 001 Lisboa, Portugal.
[c] Institut Laue-Langevin, 38000 Grenoble, France.
[d] Institute of Chemical Sciences, School of Engineering and Physical Sciences, Heriot-Watt University, Edinburgh, EH14 4AS, U.K.
[e] ISIS Neutron and Muon Source, Harwell Campus, Didcot, OX11 0QX, UK.

Experimental Details

General methods

All ILs investigated were prepared in house, utilising the methodologies reported in the SI, which were developed from those previously reported.[1,2]

Density Measurements

Density measurements used an Anton Paar DSA 5000 vibrating tube densitometer at 20 °C, calibrated according to the manufacturer's protocol and each data point was calculated from the average of multiple runs. The manufacturer's specification of accuracy in the measurements is ±1 μg cm^{-3} and their specified temperature accuracy is given as ±1 mK.

Viscosity Measurements

The viscosity was measured with a programmable Brookfield rotational rheometer RVDV-II+Pro (cone and plate version) with temperature control (temperature accuracy ±1 K) using a cryostat. A Brookfield silicone fluid (97 mPa s, 298 K) was used as a NIST-traceable viscosity standard. The viscosity data were collected between 298 K and 328 K using a CP-40 cone. The sample volume used for each experiment was ~0.5 mL. The viscosity accuracy was ±1.0 % of the full-scale viscosity range (FSVR), which has been calculated using the equation FSVR [mPa s] = (TK × SMC × 10,000)/RPM (where TK is the DV-II+Pro torque constant and SMC is the spindle multiplier constant). All fluids measured showed Newtonian behaviour at 293 K within the range of shear rate examined (7.50-712.50 s^{-1}).

Karl Fischer Titration

Water content was measured for the pure ILs, using a C20S Compact Karl Fischer Coulometric Titrator. Known quantities of the pure ILs were dissolved in known volumes of CH_2Cl_2, and water contents for the solutions were compared to that of the solvent used to prepare them to allow the water content of the ILs to be calculated. The error reported by the manufacturer is ±0.1 μg.

Surface tension Measurements

Surface tension measurements of the $[C_{10}MIM]_{1-x}[C_8MIM\text{-}F_{13}]_x[Tf_2N]$ mixtures were recorded using a Dataphysics OCA 25 tensiometer employing the pendant drop method, using drop-shape-analysis software. The manufacturer's specified resolution and accuracy for this instrument is 0.01 mNm^{-1} and 0.3 mN m^{-1}, respectively. For each sample, analysis was performed 10 times. Calibration of the pendant drop tensiometer was performed through measurements of the surface tension of Milli-Q water at 296 K. For all measurements, disposable flat-topped needles of outer diameter 1.820 mm were used.

Small-angle neutron scattering measurements

Small-angle neutron scattering (SANS) measurements were carried out at the Institut Laue-Langevin (ILL, Grenoble, France) on the recently upgraded D16 instrument, a cold neutron diffractometer, which uses a highly orientated pyrolytic graphite (HOPG) monochromator to focus the beam along the vertical axis. Set to a take-off angle of 85 deg. This gave access to a neutron wavelength of 4.47 Å. The nine crystals which make up the monochromator are orientated to maximise the incident neutron flux by focussing the beam to the sample. The desired *q*-range (0.015 - 1.1 $Å^{-1}$) was obtained in a single detector position via the new curved 2D MWPC ^{3}He detector developed at the ILL in the frame of the instrument upgrade.[3] Samples were measured in 1 mm path length and 1 cm wide quartz cuvettes.

The data were corrected for the sample container and instrument background, normalized to water and reduced to 1D using Mantid.[4] Raw data can be found at: 10.5291/ILL-data.9-11-2147.

Small-angle X-ray scattering measurements

Small-angle X-ray scattering (SAXS) employed a Bruker D8 Discover diffractometer equipped with a bespoke temperature-controlled, bored-graphite rod furnace, custom built at the University of York. Cu-K_α (λ= 0.154056 nm) radiation was used, generated from a 1 mS microfocus source. Diffraction patterns were recorded on a 2048 x 2048-pixel Bruker VANTEC 500 area detector set at a distance of 121 mm from the sample, allowing simultaneous collection of small- and wider-angle scattering data. Mixtures used employed only hydrogenous components.

Fitting of the data was carried out using SASView,[5] employing several Lorentzian peaks to describe the observed scattering peaks, with multiple iterations being summed to obtain the best fit to the data (Tables S6 & S7). In some cases, an Ornstein-Zernicke model (described as “Lorentzian” within the software) or a sphere model was also applied, when the background was not flat.

Synthesis of the Ionic Liquids

Synthetic methodologies

Air-sensitive experimental procedures were carried out under an inert nitrogen atmosphere using standard Schlenk line and glovebox techniques. Acetonitrile, hexane and toluene were purified using an Innovative Technologies anhydrous solvent engineering system. 1-Methylimidazole was dried over calcium hydride and vacuum distilled. 1-Bromooctane was dried over activated molecular sieves and distilled immediately prior to use. ^{1}H and ^{19}F NMR spectra were acquired at 293 K on a JEOL ECX-400 instrument.

Synthesis of [C_8MIM]Br

This product was prepared according to the literature method.[1] 1-Methyl imidazole (64 mL, 0.8 mol) was added to a solution of freshly distilled 1-bromooctane (148.25 g, 0.77 mol) in dry toluene (150 mL) and heated to 60 ^oC under an inert atmosphere overnight. Toluene was removed with a syringe and under vacuum at elevated temperatures for 7 days. Some excess 1-methylimidazole remained, this is removed in the metathesis (198.54 g, 96% yield). ^{1}H NMR (400 MHz, acetone-d^6, 293 K), δ (ppm): 10.23 (s, 1H), 7.94 (m, 1H), 7.87 (m, 1H), 4.45 (t, 2H), 4.10 (s, 3H), 1.94 (quint ,2H), 1.29 (m, 10H), 0.86 (t, 3H).

Synthesis [C_8MIM][Tf_2N]

The synthetic route to this product was adapted from the literature method.[1] [C_8MIM]Br (50 g, 0.18 mol) in dichloromethane (300 mL) was added to a solution of Li[Tf_2N] (68 g, 0.24 mol) in deionised water (300 mL) and stirred for two days at room temperature. The DCM layer, containing the IL, was separated and washed (3 x 200 mL) deionised water. Two subsequent negative tests for halide with $AgNO_3$ were required to ensure removal of LiBr. The DCM was removed using rotary evaporation to leave the IL and this further was dried under vacuum at 60 °C. The ^{1}H NMR spectrum indicated that all DCM had been removed (78.22 g, yield: 92%). Purity was confirmed using elemental analysis.

^{1}H NMR (400 MHz, acetone-d^6, 293 K), δ (ppm): 8.94 (s, 1H), 7.71 (m, 1H), 7.65 (m, 1H), 4.33 (t, 2H), 4.01 (s, 3H), 1.91 (quint, 2H), 1.29 (m, 10H), 0.85 (t, 3H)
Elemental analysis: calc: %C, 35.37; %H, 4.88; N, 8.63. Found: C, 35.20; H, 4.75; N, 8.71.

Synthesis of [C_{10}MIM][Tf_2N]

The same methodology as was used to synthesise the [C_8MIM][Tf_2N] was applied here. [C_{10}MIM]Br was prepared from 1-bromodecane (49.04 g) and 1-methylimadozle (16.48 g) to obtain [C_{10}MIM][Br] (50.41 g). The metathesis was then carried out with [C_{10}MIM]Br (49.3 g) and Li[Tf_2N] (51.16 g) to obtain [C_{10}MIM][Tf_2N] (68.89 g).

^{1}H NMR (400 MHz, acetone-d^6, 293 K), δ (ppm) : 8.94 (s, 1H), 7.72 (s, 1H), 7.65 (s, 1H), 4.32 (t, 2H), 4.02 (s, 3H), 1.94 (quint, 2H), 1.35-1.27 (m, 14H), 0.86 (t, 3H).
Elemental analysis: calc: %C, 38.16; %H, 5.42; N, 8.35. Found: C, 38.20; H, 5.21; N, 8.26.

Synthesis of [d_{21}-C_{10}MIM][Tf_2N]

The same methodology as was used to synthesise the [C_{10}MIM][Tf_2N] was applied here. [d_{21}-C_{10}MIM]Br was prepared from deuterated 1-bromodecane (provided by the ISIS deuteration lab) (2.63 g) and 1-methylimadozle (0.97 g) to obtain [d_{21}-C_{10}MIM][Br] (3.0 g). The metathesis was then carried out with [C_{10}MIM]Br (49.3 g) and Li[Tf_2N] (3.0 g) to obtain [d_{21}-C_{10}MIM][Tf_2N] (2.76 g).

^{1}H NMR (400 MHz, acetone-d^6, 293 K), δ (ppm) : 9.02 (s, 1H), 7.77 (s, 1H), 7.70 (s, 1H), 4.06 (s, 3H)
Deuteration level >97% from NMR.

Synthesis [C_8MIM-F_{13}]I

This product was prepared according to the literature method.[1] 1-Methylimidazole (7 mL, 7.21 g, 0.088 mol) was added to a solution of *1H,1H,2H,2H*-perfluorooctyl iodide (23.5 mL, 45.5 g, 0.096 mol) in acetonitrile (150 mL). The resulting solution was heated to 60 ^{o}C and stirred under an inert N_2 atmosphere for 3 weeks, with progression monitored using ^{1}H and ^{19}F NMR. The acetonitrile was removed under vacuum. The resulting solid was washed with dry hexane (3 x 50 mL) to removes excess *1H,1H,2H,2H*-perfluorooctyl iodide. The solid was dried under vacuum (35.22 g, 72% yield). Remaining impurities are removed during metathesis.

^{1}H NMR (400 MHz, acetone-d^6, 293 K), δ (ppm): 9.71 (s, 1H), 8.03 (m, 1H), 7.84 (m, 1H), 4.92 (t, 2H), 4.10 (s, 3H), 1.94 (quint ,2H), 1.29 (m, 10H), 0.86 (t, 3H)
^{19}F NMR (376 MHz, acetone-d^6, 293 K) δ (ppm): -81.5 (3F), -114.3 (2F), -122.3 (2F), -123.3 (2F), -123.9 (2F), -126.7 (2F)

Synthesis [C_8MIM-F_{13}][Tf_2N]

The synthetic route to this product was adapted from the literature method.[1] The solid [C_8MIM-F_{13}]I (34.72 g, 0.062 mol) was dissolved in DCM (200 mL) and added to a solution of Li[Tf_2N] (20.83 g, 0.073 mol) in deionised water (200 mL) and stirred at room temperature for 2 days. The DCM layer, containing the IL, was separated and washed (5 x 200 mL) deionised water. Two subsequent negative tests for halide with $AgNO_3$ were required to ensure removal of LiI. DCM was removed using rotary evaporation and the IL was dried under vacuum at 60 ^{o}C to afford a dark amber oil (26.80 g, 61% yield). Purity of the compound was confirmed by elemental analysis.

^{1}H NMR (400 MHz, acetone-d^6, 293 K), δ (ppm): 9.12 (s, 1H), 7.88 (m, 1H), 7.72 (m, 1H), 4.81 (t, 2H), 4.04 (s, 3H), 3.11 (m, 2H)
^{19}F NMR (376 MHz, acetone-d^6, 293 K) δ (ppm):-79.9 (6F), -81.7 (3F), -114.6 (2F), -122.4 (2F), -123.5 (2F), -124.2 (2F), -126.9(2F)
Elemental analysis: calc: %C, 23.70; %H, 1.42; N, 5.93. Found: C, 23.58; H, 1.28; N, 5.54.

Synthesis of [C_{10}MIM-F_{17}][Tf_2N]

The same methodology as was used to synthesise the [C_8MIM-F_{13}][Tf_2N] was applied here. [C_{10}MIM-F_{17}]I was prepared from *1H,1H,2H,2H*-perfluorodecyl iodide (50 g) and 1-methylimadozle (7 g) to obtain [C_{10}MIM-F_{17}]I (36.25 g). The metathesis was then carried out with [C_{10}MIM-F_{17}]I (35.75) and Li[Tf_2N] (17.2 g) to obtain [C_{10}MIM-F_{17}][Tf_2N] (32.67 g).

^{1}H NMR (400 MHz, acetone-d^6, 293 K), δ (ppm): 9.17 (s, 1H), 7.91 (m, 1H), 7.72 (m, 1H), 4.81 (t, 2H), 4.06 (s, 3H), 3.09 (m, 2H)

^{19}F NMR (376 MHz, acetone-d^6, 293 K) δ (ppm) :-80.0 (6F), -81.6 (3F), -114.4 (2F), -122.13 (2F), -122.4 (4F), -123.3 (2F), -124.0 (2F), -126.7(2F)

Elemental analysis: Elemental analysis: calc: %C, 23.74; %H, 1.25; N, 5.19. Found: C, 23.54; H, 1.05; N, 5.25.

Density data

Table S1: Density, excess density, molar volume and excess molar volume data at 293.15 K for the $[C_{10}MIM]_{1-x}[C_8MIM\text{-}F_{13}]_x[Tf_2N]$ IL mixtures

x	**M/ g mol^{-1}**	**ρ / g cm^{-3}**	**Δρ / %**	**V_m / cm^{3}mol^{-1}**	**ΔV_m / %**
0.00	503.52	1.28		392.59	
0.05	513.81	1.30	-0.007	393.82	0.082
0.20	544.69	1.37	0.061	396.91	0.176
0.35	575.56	1.44	-0.030	400.32	0.349
0.50	606.44	1.50	-0.071	403.27	0.404
0.65	637.31	1.57	0.150	404.92	0.138
0.80	668.18	1.63	-0.228	408.79	0.421
0.95	699.06	1.70	-0.098	410.42	0.153
1.00	709.35	1.73		392.59	

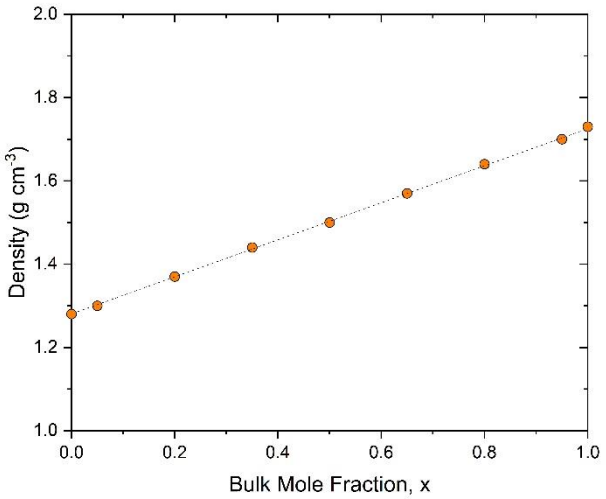

Figure S1: Plot of density for mixtures $[C_{10}MIM]_{1-x}[C_8MIM\text{-}F_{13}]_x[Tf_2N]$ at 20 °C; errors are small and within the markers. Dotted line is the expected density based on a linear combination of the densities of the two components.

Viscosity

Table S2: Viscosity data for the IL mixture $[C_{10}MIM]_{1-x}[C_8MIM\text{-}F_{13}]_x[Tf_2N]$ in the temperature range between 298 and 328 K

x	**Viscosity, mPa s**						
	T, K						
	298	**303**	**308**	**313**	**318**	**323**	**328**
0.00	119.72	92.58	72.59	58.04	47.18	38.06	32.05
0.05	124.85	95.89	75.00	59.68	48.13	38.60	32.44
0.20	160.66	125.22	96.75	76.01	60.68	47.79	39.67
0.35	211.22	161.65	123.21	95.30	75.12	58.55	47.96
0.50	288.12	219.77	164.69	126.15	97.98	74.44	60.82
0.65	424.73	306.73	225.75	169.62	129.47	97.45	78.43
0.80	642.62	454.79	327.95	241.49	181.88	133.87	106.21
0.95	977.61	680.39	480.63	346.21	254.42	183.70	143.41
1.00	1049.45	716.68	504.45	364.17	268.47	195.98	153.04

SANS data fitting models

Teubner-Strey model

$$I(q) = \frac{1}{a + c_1 q^2 + c_2 q^4} + background$$

Here *a, c*$_1$ and *c*$_2$ are fitting parameters which can be used to yield the *d*-spacing, correlation length (x_i) and amphiphile strength (γ) parameter.

$$d\ spacing = \frac{2\pi}{\sqrt{0.5\sqrt{a/c_2} - c_1/4c_2}} \qquad x_i = \frac{1}{\sqrt{0.5\sqrt{a/c_2} + 0.25 c_1/c_2}} \qquad \gamma = \frac{c_1}{\sqrt{4ac_2}}$$

The *d*-spacing relates to the periodic distance present in the lamellar or bicontinuous structure if such structure is not present it instead relates to the distance between scattering objects. The correlation length relates to the size of the scattering objects. The amphiphilic strength parameter indicates the nature of the structure present. When $\gamma > 1$ the system is considered to be disordered, when $1 > \gamma > 0$ then aggregates are present, when $0 > \gamma > -1$ a bicontinuous/ percolated structure is present and when $\gamma < -1$ lamellar structure is present.

Where $0 < \gamma < 1$, the *d*-spacing is related to the distance between the aggregates, while the correlation length is associated with the density fluctuations within the aggregates, which can be interpreted as the alkyl chain aggregate size. Where $-1 < \gamma < 0$, the *d*-spacing relates to the local bilayer dimension (given by the position of the PNPP and Bragg's law), while the correlation length relates to the alkyl chain domain length scale. The point at which the amphiphile strength changes from negative to positive values is known as the Lifshitz line.

This model does not give good fits across the full compositional range of these mixtures. To achieve better fits either Lorentzian peaks, a spherical model or Ornstein-Zernicke model, or a combination of the peaks with one of the other two models.

Spherical model:

The simplest form factor model which can be applied is a spherical model with uniform SLD across the sphere. It can be described by:

$$P(q) = \frac{Scale}{V}\left[\frac{3V\,(\Delta\rho) - qrcos(qr)}{(qr)^2}\right]^2 + bkg$$

Where V is the volume of the scatterer, scale is a volume fraction, r is the radius and Δρ is the difference between the scattering length density of the scatterer and the dispersion medium.

$$I(q) = n\Delta\rho^2 V^2 P(q) S(q) + B$$

where $I(q)$ is the intensity of the scattered neutrons, n is the number of scatterers, $\Delta\rho$ is the difference in SLD between the scatterer and the dispersion medium, V is the volume of particles, $P(q)$ is the form factor, $S(q)$ is the structure factor and B is the background.

Fitting parameters

$[C_{10}MIM]_{1-x}[C_{10}MIM]_x[Tf_2N]$
Teubner-Strey

Table S3: Parameters used for fitting $[C_{10}MIM]_{1-x}[C_{10}MIM\text{-}F_{17}]_x[Tf_2N]$ data to Teubner- Strey model

x	Domain size, Å	Correlation Length, Å
$[C_{10}MIM][Tf_2N]$	20.8	11.3
0.05	21.0	10.0
0.20	21.5	7.2
0.35	44.0	4.0
0.50	44.0	4.7
0.65	35.0	4.7
0.80	31.0	5.1
0.95	25.0	12.5
$[C_{10}MIM\text{-}F_{17}][Tf_2N]$	25.0	15.5

Spherical model and Lorentzian peaks

Table S4: Parameters used for fitting $[C_{10}MIM]_{1-x}[C_{10}MIM\text{-}F_{17}]_x[Tf_2N]$ data to a sphere + Lorentzian model, along with the peak positions of the three peaks seen in the scattering data.

x	Radius / Å	PNPP / $Å^{-1}$	COP / Å	CP / Å
$[C_{10}MIM][Tf_2N]$	-	0.28	0.83	1.34
0.05	-	0.28	0.83	1.33
0.2	12.0	0.28	0.84	1.26
0.35	12.0	0.28	0.86	1.22
0.5	10.8	0.28	0.86	1.21
0.65	7.8	0.27	0.88	1.17
0.8	7.7	0.24	0.90	1.15
0.95	7.6	0.24	0.90	1.14
$[C_{10}MIM\text{-}F_{17}][Tf_2N]$	-	0.24	0.91	1.15

Fits for pure ILs

$[C_{10}MIM][Tf_2N]$

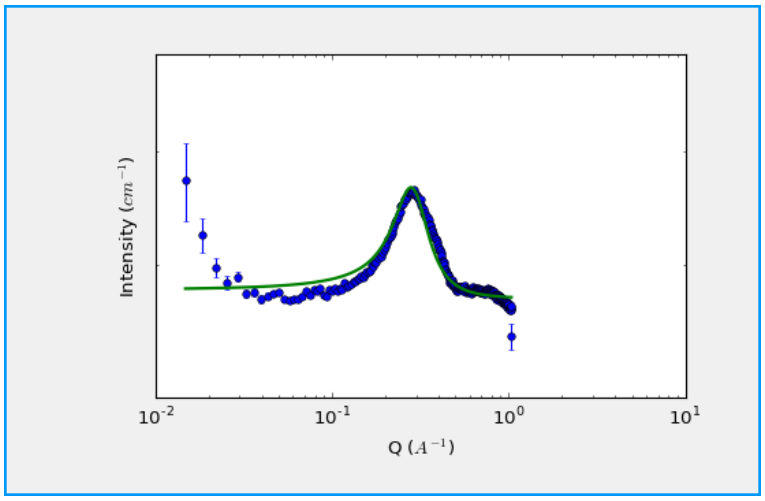

Figure S2: SANS data for $[C_{10}MIM][Tf_2N]$ fitted using a Lorentzian peak model

$[C_8MIM][Tf_2N]$

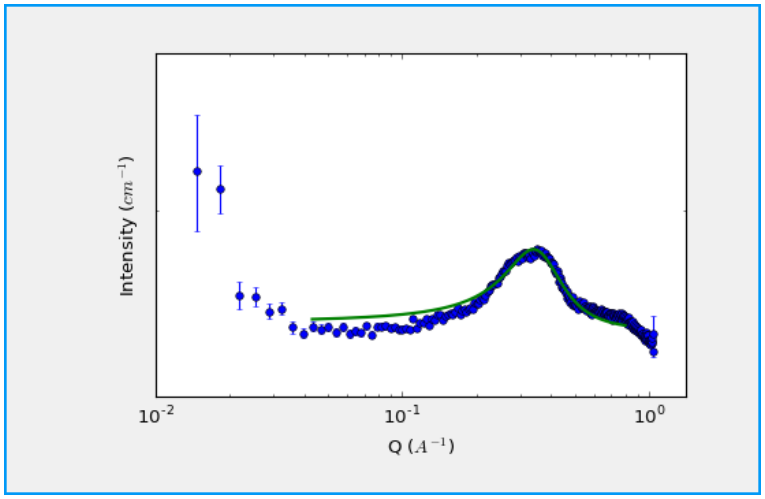

Figure S3: SANS data for $[C_8MIM][Tf_2N]$ fitted using a Lorentzian peak model

$[C_{10}MIM\text{-}F_{17}][Tf_2N]$

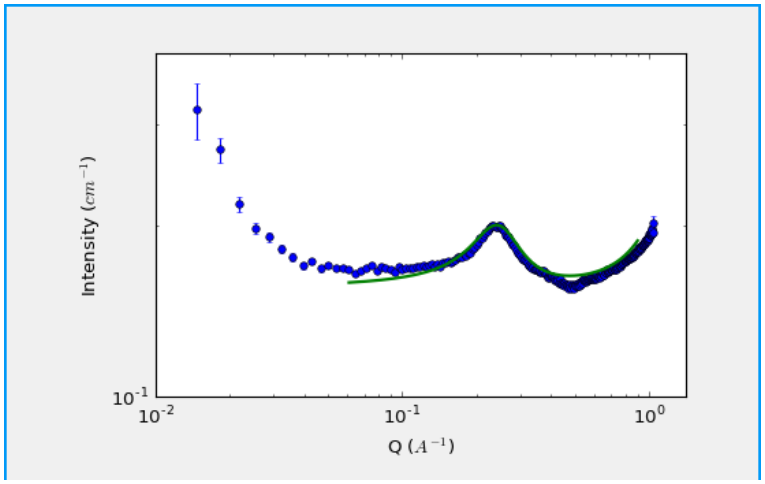

Figure S4: SANS data for $[C_{10}MIM\text{-}F_{17}][Tf_2N]$ fitted using Lorentzian peak models

$[C_8MIM\text{-}F_{13}][Tf_2N]$

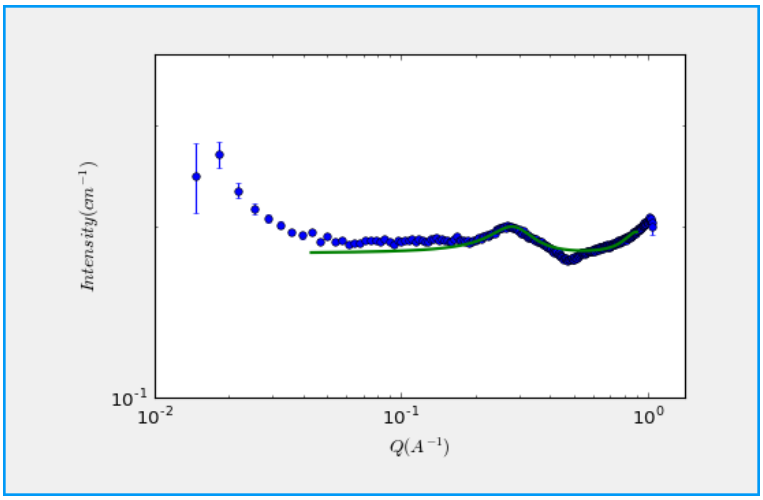

Figure S5: SANS data for $[C_8MIM\text{-}F_{13}][Tf_2N]$ fitted using Lorentzian peak models

Fits for $[C_{10}MIM]_{1-x}[C_{10}MIM\text{-}F_{17}]_x[Tf_2N]$

$[C_{10}MIM]_{0.95}[C_{10}MIM\text{-}F_{17}]_{0.05}[Tf_2N]$

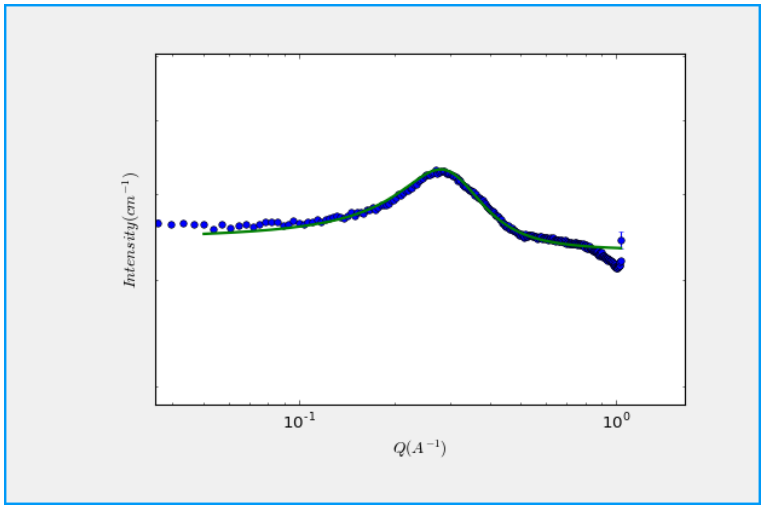

Figure S6*:* SANS data for $[C_{10}MIM]_{0.95}[C_{10}MIM\text{-}F_{17}]_{0.05}[Tf_2N]$ fitted using a Lorentzian peak model

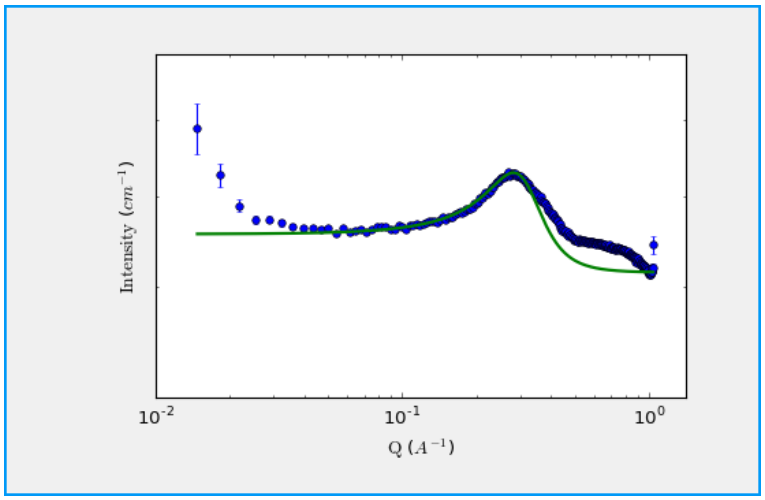

Figure S7: SANS data for $[C_{10}MIM]_{0.95}[C_{10}MIM\text{-}F_{17}]_{0.05}[Tf_2N]$ fitted using a Teubner Strey model

$[C_{10}MIM]_{0.8}[C_{10}MIM\text{-}F_{17}]_{0.2}[Tf_2N]$

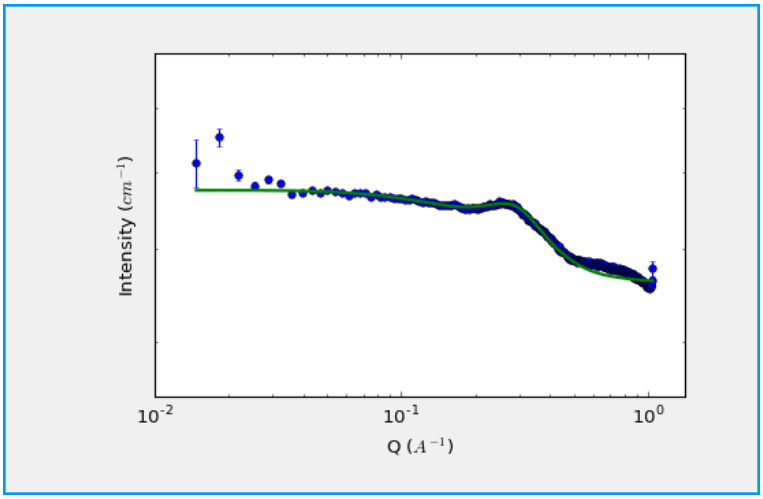

Figure S8: SANS data for $[C_{10}MIM]_{0.8}[C_{10}MIM\text{-}F_{17}]_{0.2}[Tf_2N]$ fitted using a Spherical and Lorentzian peak model

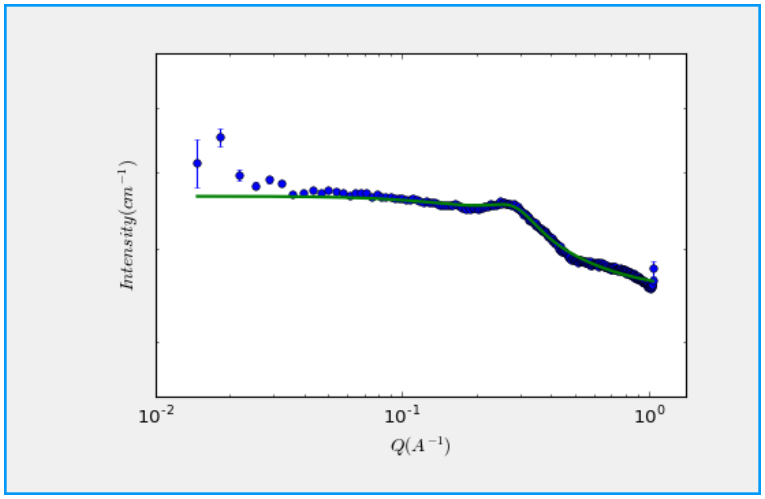

Figure S9: SANS data for $[C_{10}MIM]_{0.8}[C_{10}MIM\text{-}F_{17}]_{0.2}[Tf_2N]$ fitted using a Ornstein-Zernike model and Lorentzian peak model

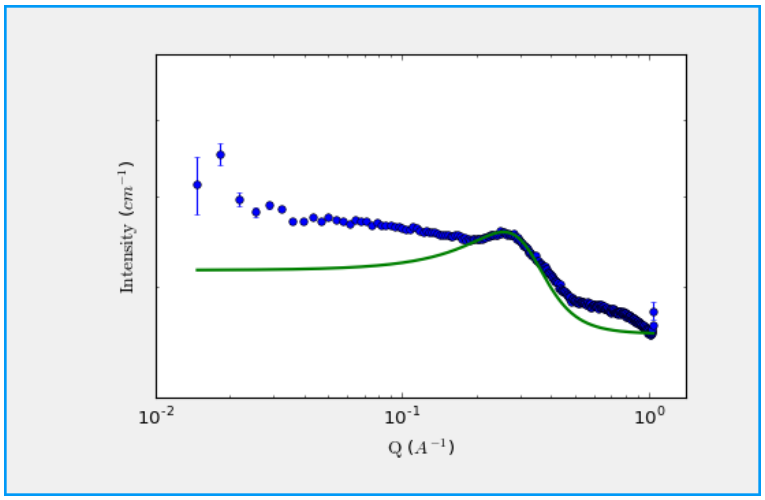

Figure S10: SANS data for $[C_{10}MIM]_{0.8}[C_{10}MIM\text{-}F_{17}]_{0.2}[Tf_2N]$ fitted using a Teubner-Strey model

$[C_{10}MIM]_{0.65}[C_{10}MIM\text{-}F_{17}]_{0.35}[Tf_2N]$

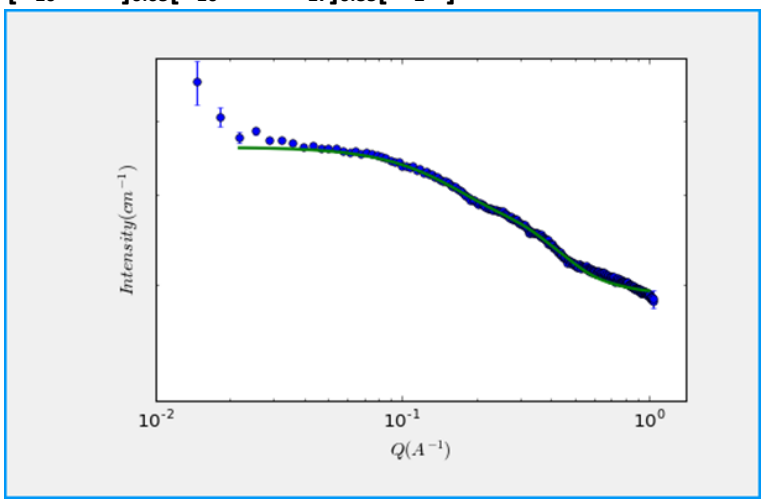

Figure S11: SANS data for $[C_{10}MIM]_{0.65}[C_{10}MIM\text{-}F_{17}]_{0.35}[Tf_2N]$ fitted using a Spherical and Lorentzian peak model

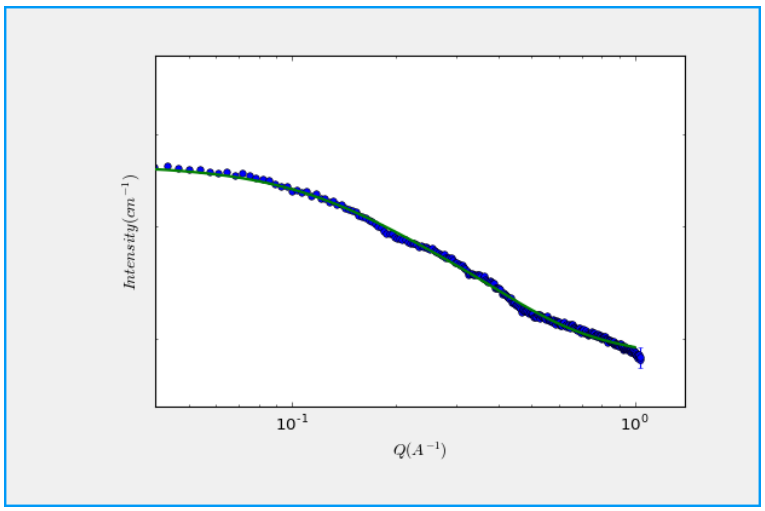

Figure S12: SANS data for $[C_{10}MIM]_{0.65}[C_{10}MIM\text{-}F_{17}]_{0.35}[Tf_2N]$ fitted using a Ornstein-Zernike model and Lorentzian peak

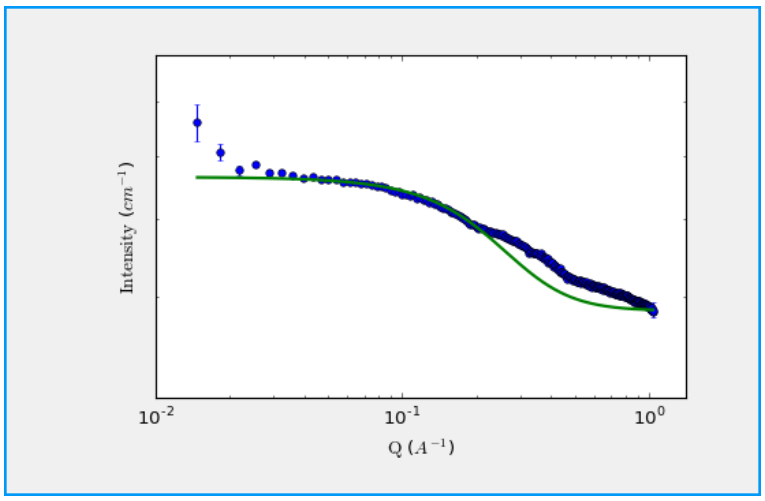

Figure S13: SANS data for $[C_{10}MIM]_{0.65}[C_{10}MIM\text{-}F_{17}]_{0.35}[Tf_2N]$ fitted using a Teubner-Strey model

$[C_{10}MIM]_{0.5}[C_{10}MIM\text{-}F_{17}]_{0.5}[Tf_2N]$

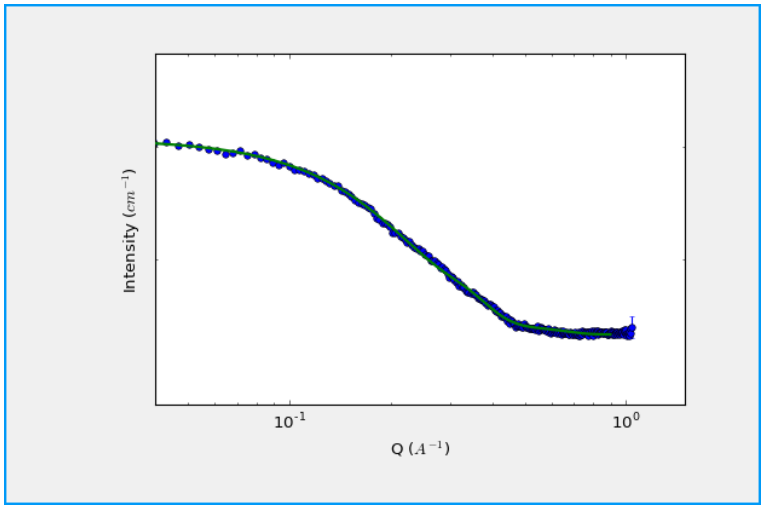

Figure S14: SANS data for $[C_{10}MIM]_{0.5}[C_{10}MIM\text{-}F_{17}]_{0.5}[Tf_2N]$ fitted using a Spherical and Lorentzian peak model

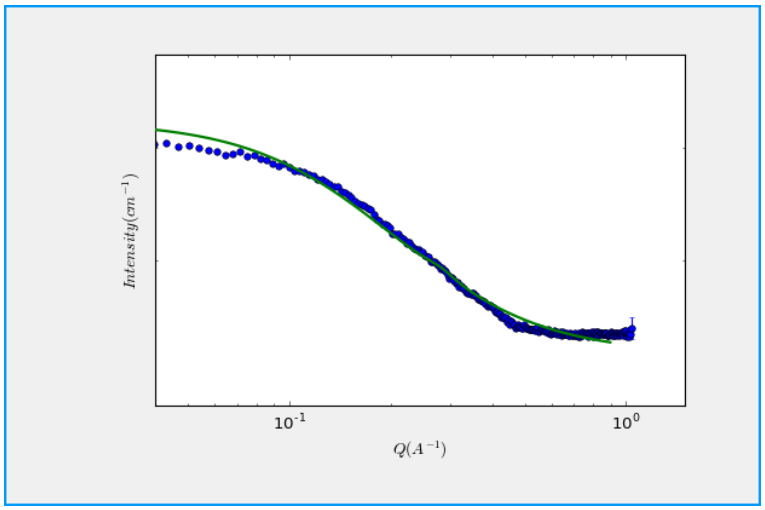

Figure S15: SANS data for $[C_{10}MIM]_{0.5}[C_{10}MIM\text{-}F_{17}]_{0.5}[Tf_2N]$ fitted using a Ornstein-Zernike model

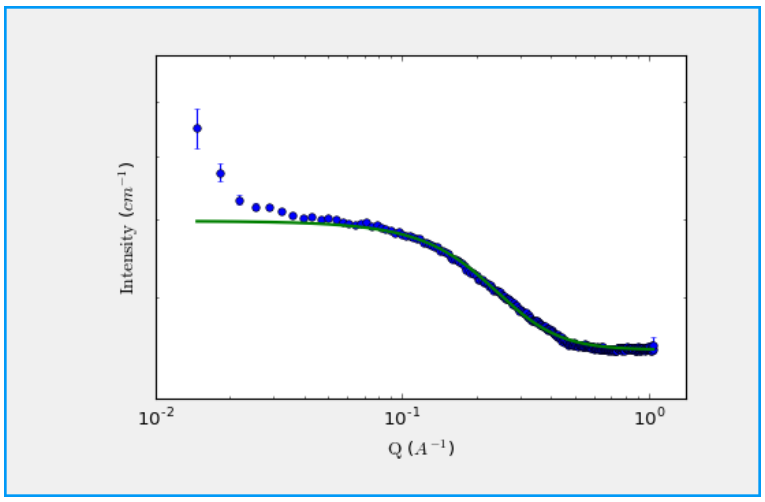

Figure S16: SANS data for $[C_{10}MIM]_{0.5}[C_{10}MIM\text{-}F_{17}]_{0.5}[Tf_2N]$ fitted using a Teubner-Strey model

$[C_{10}MIM]_{0.35}[C_{10}MIM\text{-}F_{17}]_{0.65}[Tf_2N]$

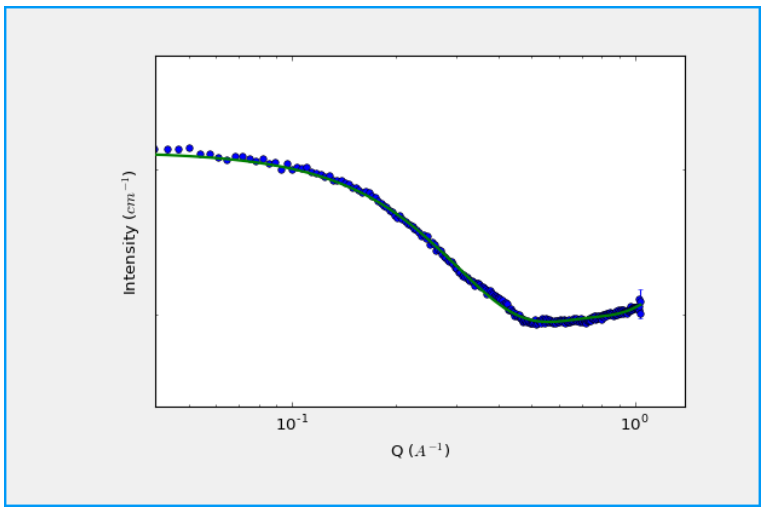

Figure S17: SANS data for $[C_{10}MIM]_{0.35}[C_{10}MIM\text{-}F_{17}]_{0.65}[Tf_2N]$ fitted using a Spherical model

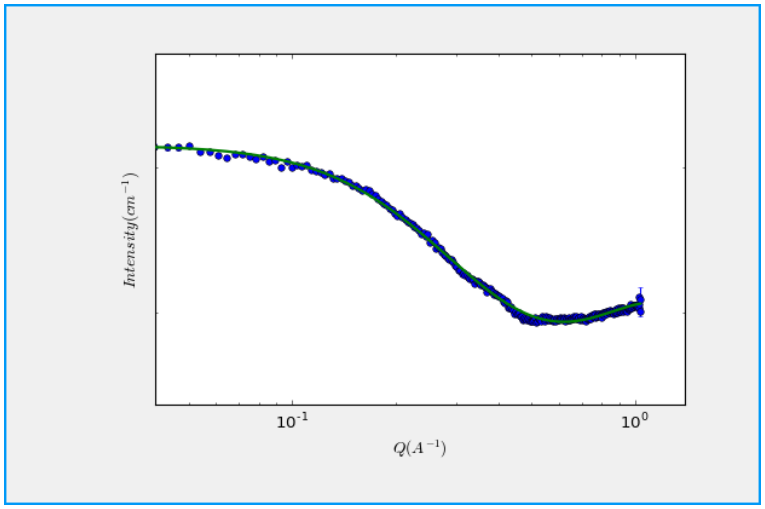

Figure S18: SANS data for $[C_{10}MIM]_{0.35}[C_{10}MIM\text{-}F_{17}]_{0.65}[Tf_2N]$ fitted using a Ornstein-Zernike model

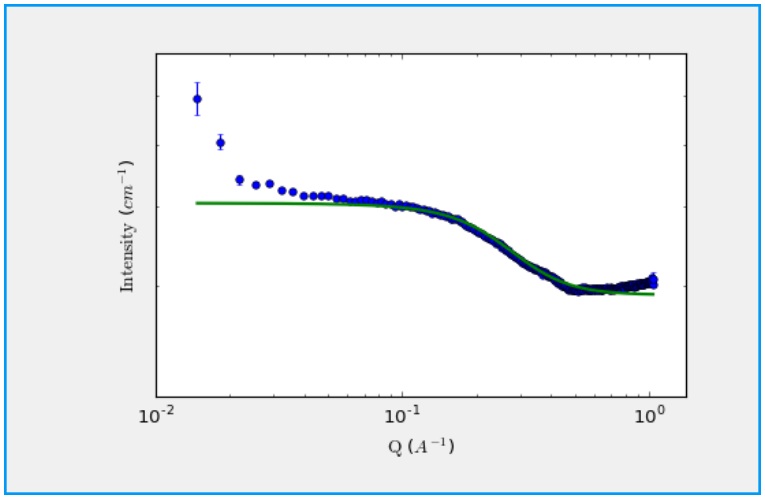

Figure S19: SANS data for $[C_{10}MIM]_{0.35}[C_{10}MIM\text{-}F_{17}]_{0.65}[Tf_2N]$ fitted using a Teubner-Strey model

$[C_{10}MIM]_{0.2}[C_{10}MIM\text{-}F_{17}]_{0.8}[Tf_2N]$

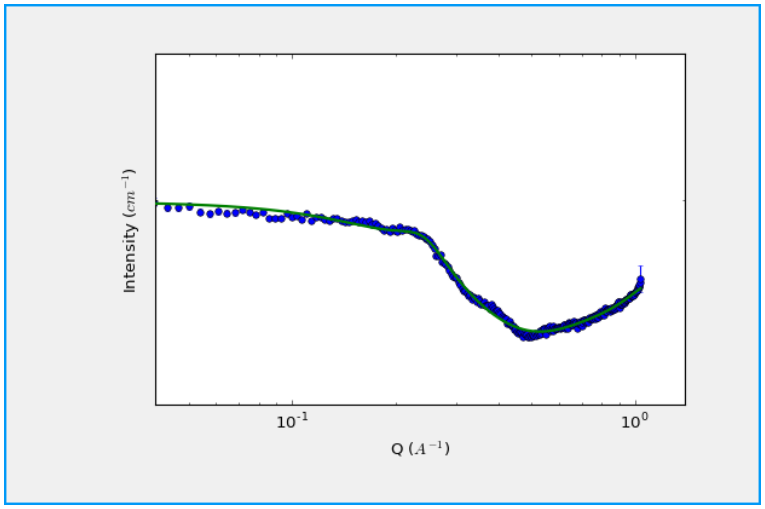

Figure S20: SANS data for $[C_{10}MIM]_{0.2}[C_{10}MIM\text{-}F_{17}]_{0.8}[Tf_2N]$ fitted using a Spherical and Lorentzian peak model

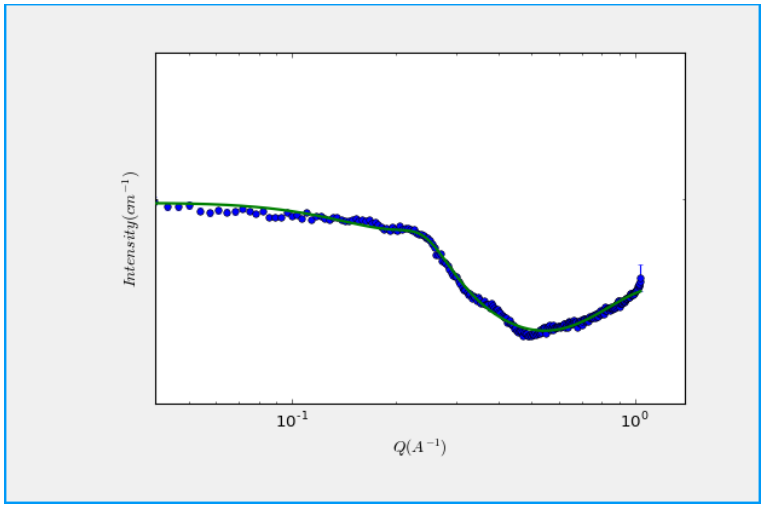

Figure S21: SANS data for $[C_{10}MIM]_{0.2}[C_{10}MIM\text{-}F_{17}]_{0.8}[Tf_2N]$ fitted using a Ornstein-Zernike and Lorentzian peak

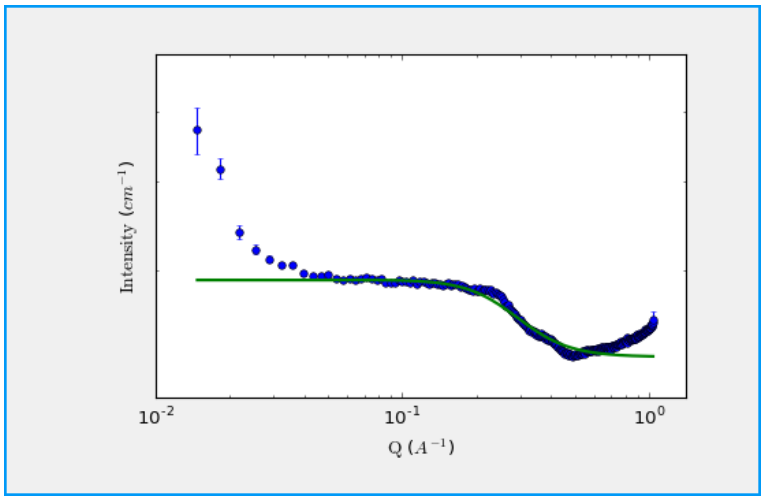

Figure S22: SANS data for $[C_{10}MIM]_{0.2}[C_{10}MIM\text{-}F_{17}]_{0.8}[Tf_2N]$ fitted using a Teubner-Strey model

$[C_{10}MIM]_{0.05}[C_{10}MIM\text{-}F_{17}]_{0.95}[Tf_2N]$

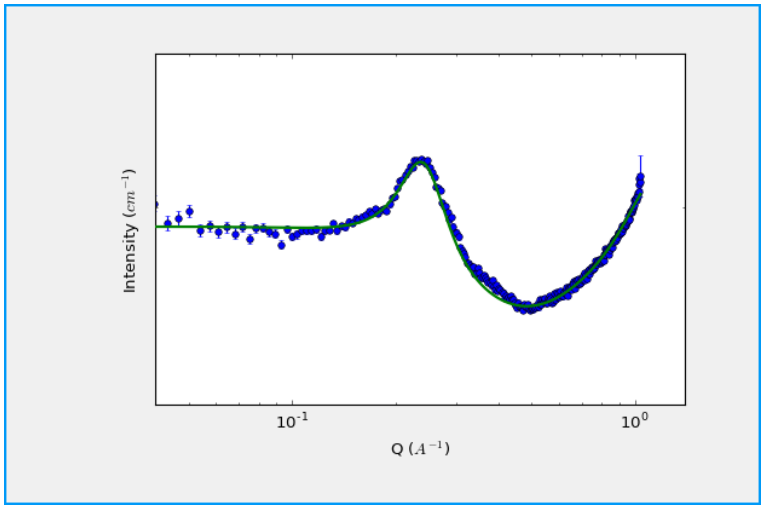

Figure S23*:* SANS data for $[C_{10}MIM]_{0.05}[C_{10}MIM\text{-}F_{17}]_{0.95}[Tf_2N]$ fitted using a Spherical and Lorentzian peak model

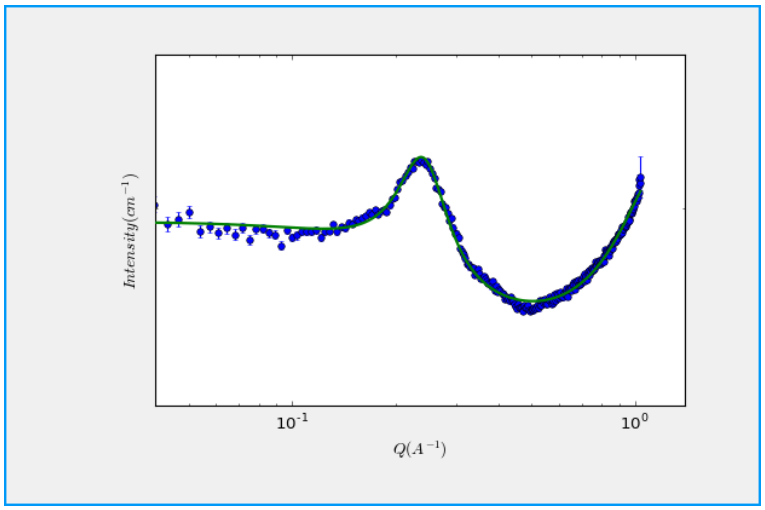

Figure S24: SANS data for $[C_{10}MIM]_{0.05}[C_{10}MIM\text{-}F_{17}]_{0.95}[Tf_2N]$ fitted using a Ornstein-Zernike and Lorentzian peak models

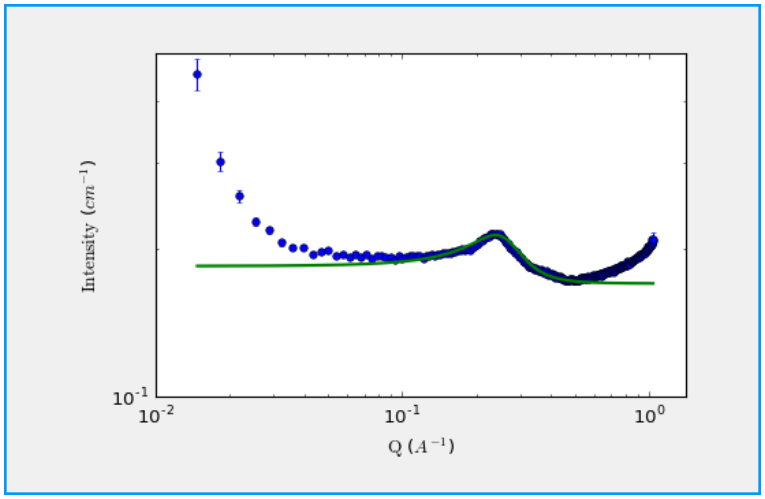

Figure S25: SANS data for $[C_{10}MIM]_{0.05}[C_{10}MIM\text{-}F_{17}]_{0.95}[Tf_2N]$ fitted using a Teubner-Strey model

Fits for $[C_{10}MIM]_{1-x}[C_8MIM\text{-}F_{13}]_x[Tf_2N]$

$[C_{10}MIM]_{0.95}[C_8MIM\text{-}F_{13}]_{0.05}[Tf_2N]$

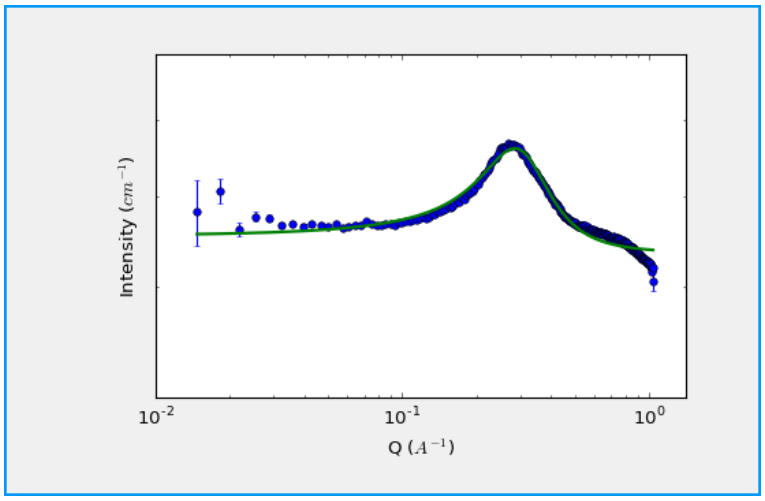

Figure S26: SANS data for $[C_{10}MIM]_{0.95}[C_8MIM\text{-}F_{13}]_{0.05}[Tf_2N]$ fitted using a Lorentzian peak model

$[C_{10}MIM]_{0.8}[C_8MIM\text{-}F_{13}]_{0.2}[Tf_2N]$

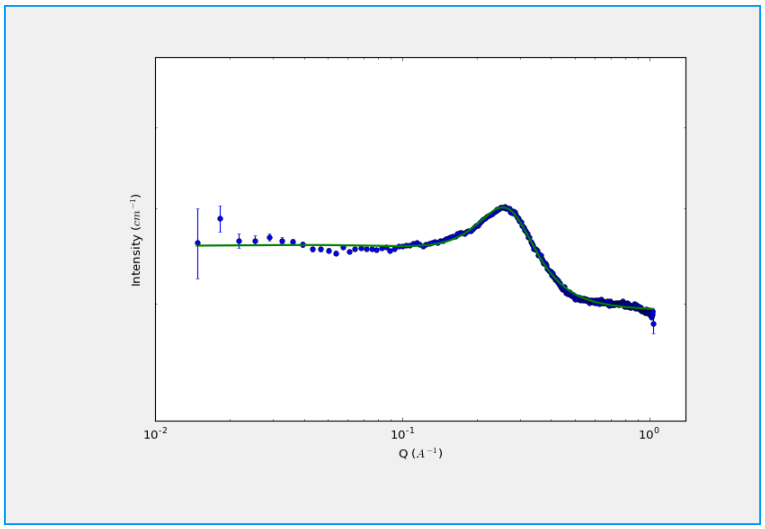

Figure S27: SANS data for $[C_{10}MIM]_{0.8}[C_8MIM\text{-}F_{13}]_{0.2}[Tf_2N]$ fitted using a Spherical model and Lorentzian peak

$[C_{10}MIM]_{0.65}[C_8MIM\text{-}F_{13}]_{0.35}[Tf_2N]$

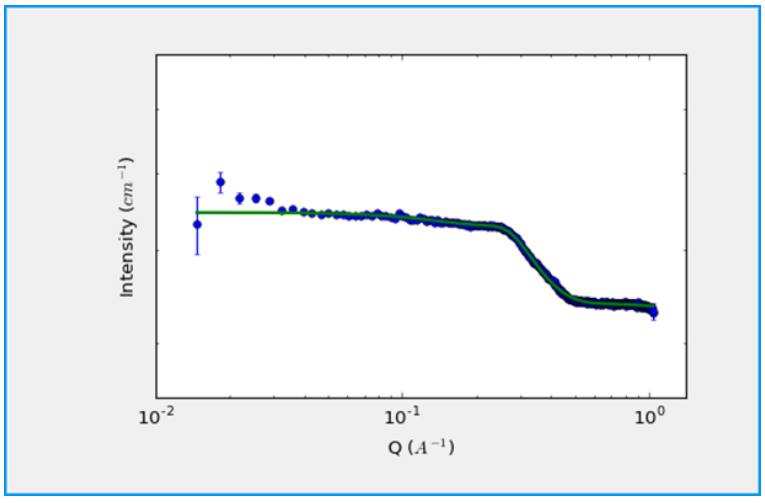

Figure S28: SANS data for $[C_{10}MIM]_{0.65}[C_8MIM\text{-}F_{13}]_{0.35}[Tf_2N]$ fitted using a Spherical model and Lorentzian peak

$[C_{10}MIM]_{0.5}[C_8MIM\text{-}F_{13}]_{0.5}[Tf_2N]$

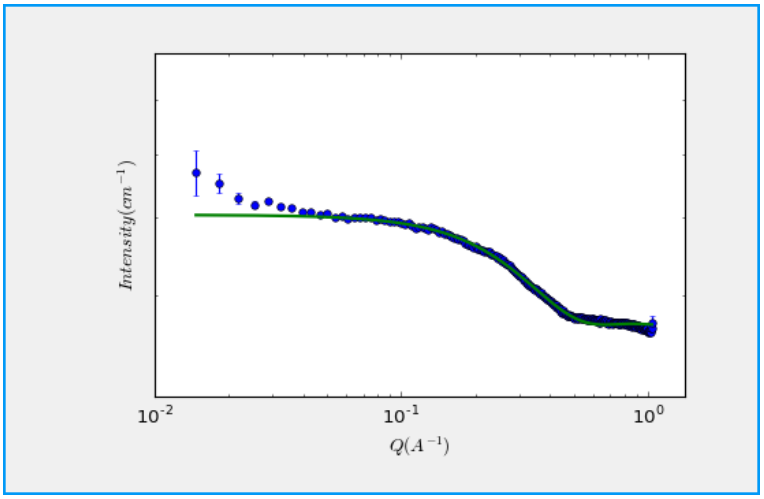

Figure S29: SANS data for $[C_{10}MIM]_{0.5}[C_8MIM\text{-}F_{13}]_{0.5}[Tf_2N]$ fitted using a Spherical model

$[C_{10}MIM]_{0.35}[C_8MIM\text{-}F_{13}]_{0.65}[Tf_2N]$

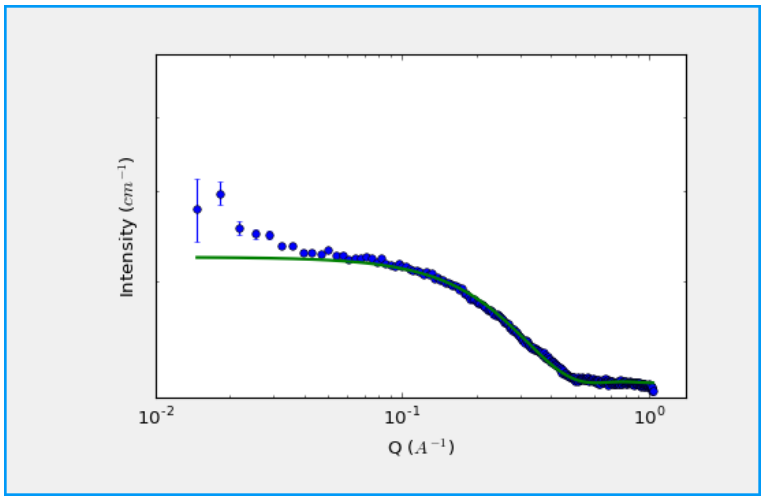

Figure S30: SANS data for $[C_{10}MIM]_{0.35}[C_8MIM\text{-}F_{13}]_{0.65}[Tf_2N]$ fitted using a Spherical model

$[C_{10}MIM]_{0.2}[C_8MIM\text{-}F_{13}]_{0.8}[Tf_2N]$

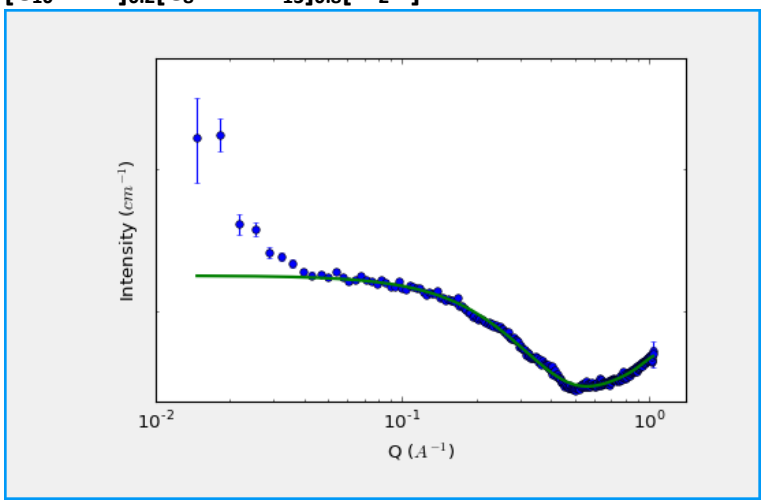

Figure S31: SANS data for $[C_{10}MIM]_{0.8}[C_8MIM\text{-}F_{13}]_{0.2}[Tf_2N]$ fitted using a Spherical model and Lorentzian peak

$[C_{10}MIM]_{0.05}[C_8MIM\text{-}F_{13}]_{0.95}[Tf_2N]$

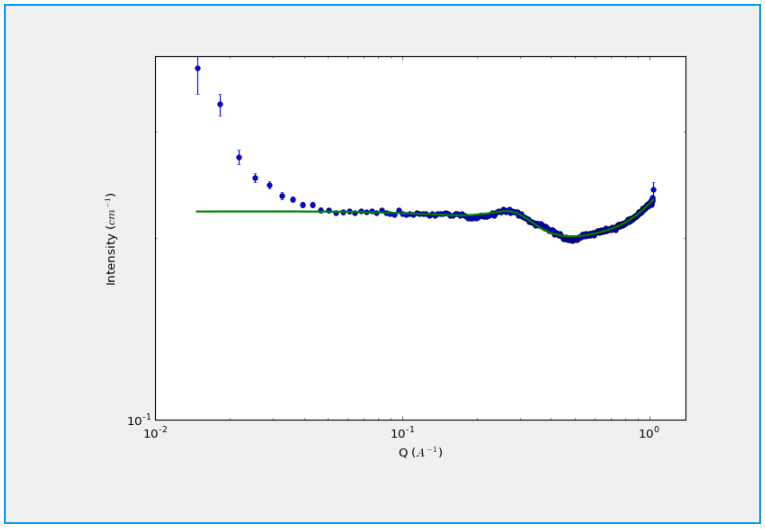

Figure S32: SANS data for $[C_{10}MIM]_{0.05}[C_8MIM\text{-}F_{13}]_{0.95}[Tf_2N]$ fitted using a Spherical model and Lorentzian peaks

Fits for $[C_8MIM]_{1\text{-}x}[C_{10}MIM\text{-}F_{17}]_x[Tf_2N]$

$[C_8MIM]_{0.95}[C_{10}MIM\text{-}F_{17}]_{0.05}[Tf_2N]$

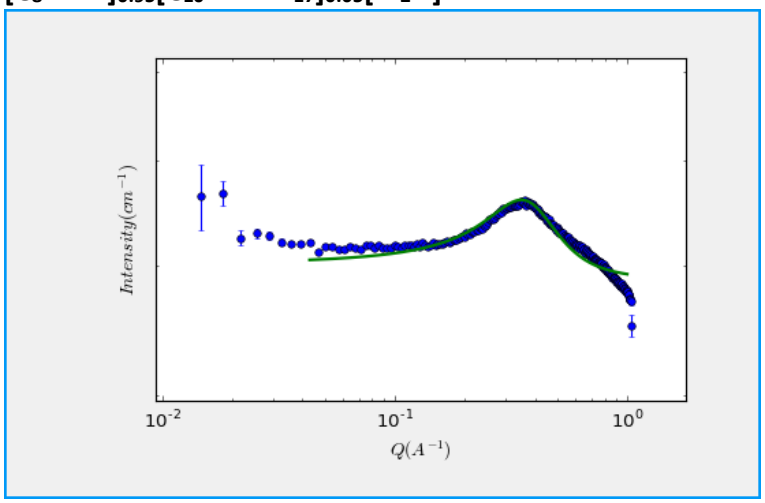

Figure S33*:* SANS data for $[C_8MIM]_{0.95}[C_{10}MIM\text{-}F_{17}]_{0.05}[Tf_2N]$ fitted using a *Lorentzian peak*

$[C_8MIM]_{0.8}[C_{10}MIM\text{-}F_{17}]_{0.2}[Tf_2N]$

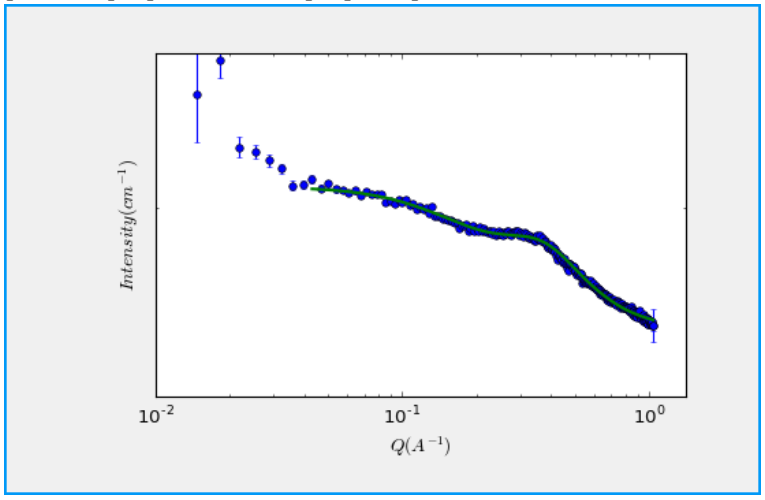

Figure S34: SANS data for $[C_8MIM]_{0.8}[C_{10}MIM\text{-}F_{17}]_{0.2}[Tf_2N]$ fitted using a Spherical model and Lorentzian peak

$[C_8MIM]_{0.65}[C_{10}MIM\text{-}F_{17}]_{0.35}[Tf_2N]$

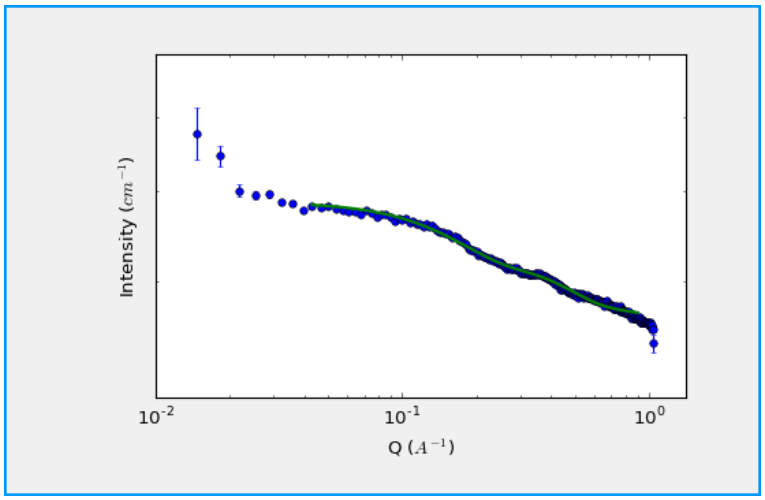

Figure S35: SANS data for $[C_8MIM]_{0.65}[C_{10}MIM\text{-}F_{17}]_{0.35}[Tf_2N]$ fitted using a Spherical model and Lorentzian peak

$[C_8MIM]_{0.5}[C_{10}MIM\text{-}F_{17}]_{0.5}[Tf_2N]$

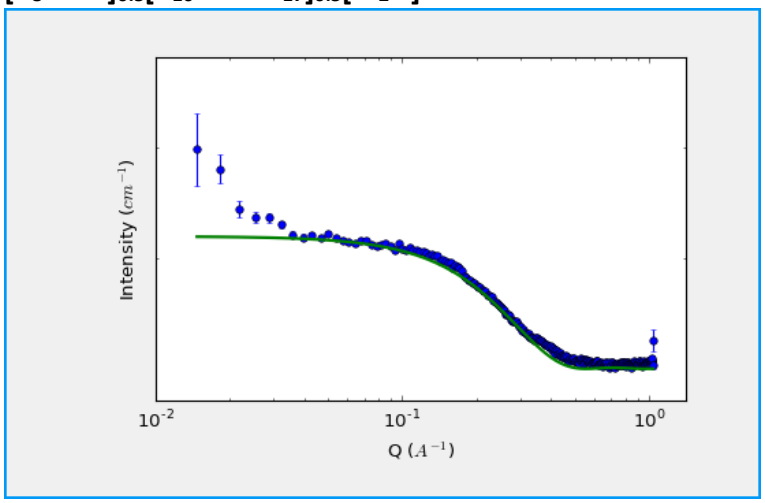

Figure S36: SANS data for $[C_8MIM]_{0.5}[C_{10}MIM\text{-}F_{17}]_{0.5}[Tf_2N]$ fitted using a Spherical model

$[C_8MIM]_{0.35}[C_{10}MIM\text{-}F_{17}]_{0.65}[Tf_2N]$

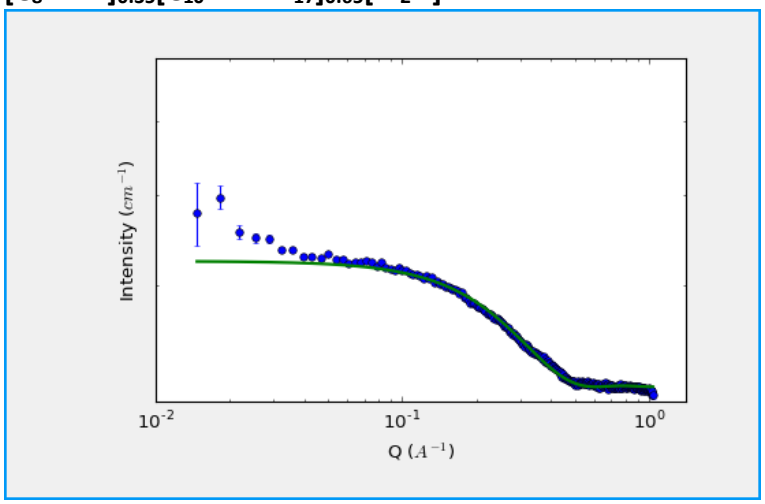

Figure S37: SANS data for $[C_8MIM]_{0.35}[C_{10}MIM\text{-}F_{17}]_{0.65}[Tf_2N]$ fitted using a Spherical model

$[C_8MIM]_{0.2}[C_{10}MIM\text{-}F_{17}]_{0.8}[Tf_2N]$

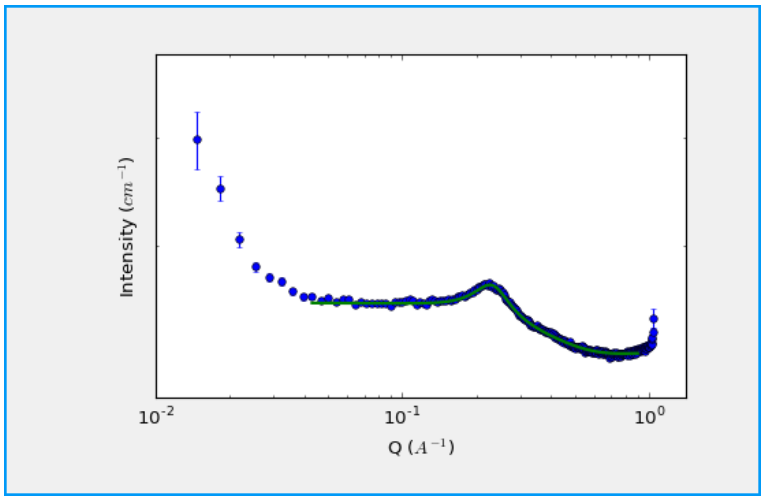

Figure S38: SANS data for $[C_8MIM]_{0.2}[C_{10}MIM\text{-}F_{17}]_{0.8}[Tf_2N]$ fitted using a Spherical model and Lorentzian peak

$[C_8MIM]_{0.05}[C_{10}MIM\text{-}F_{17}]_{0.95}[Tf_2N]$

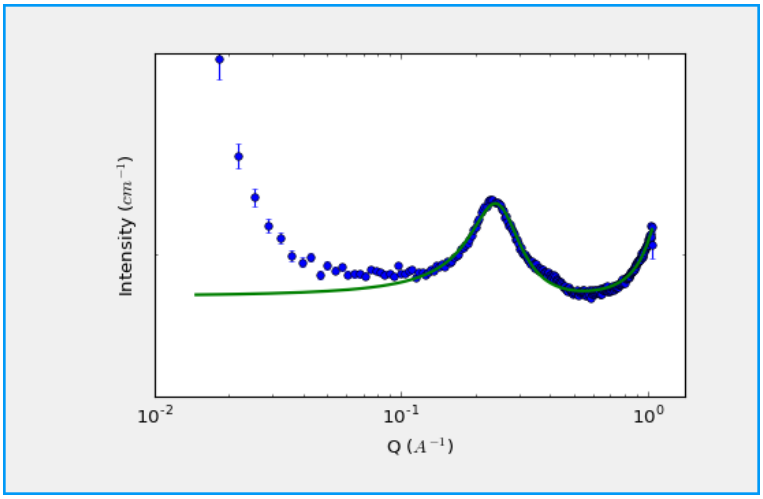

Figure S39: SANS data for $[C_8MIM]_{0.95}[C_{10}MIM\text{-}F_{17}]_{0.05}[Tf_2N]$ fitted using a Lorentzian peaks

Effect of Temperature on scattering

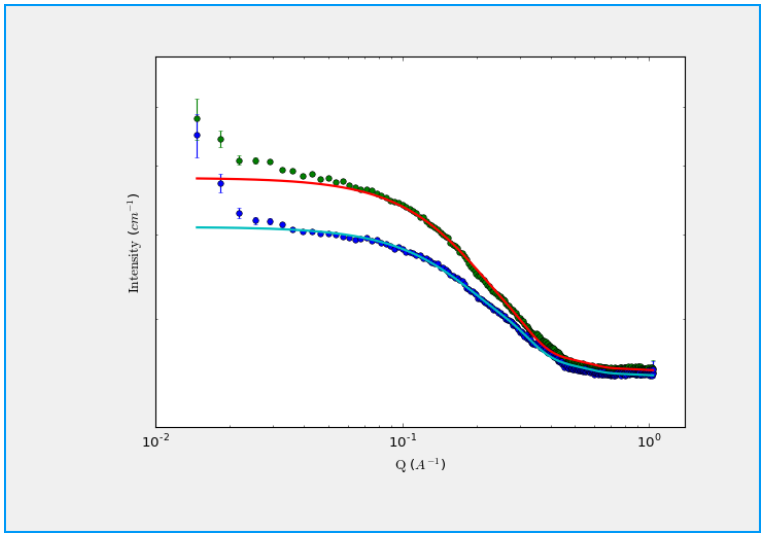

Figure S40: Example of SANS data, $[C_{10}MIM]_{0.5}[C_{10}MIM\text{-}F_{17}]_{0.5}[Tf_2N]$, at 20 °C (green) and 60 °C (blue) fitted with the same parameters (allowing scale and background to vary)

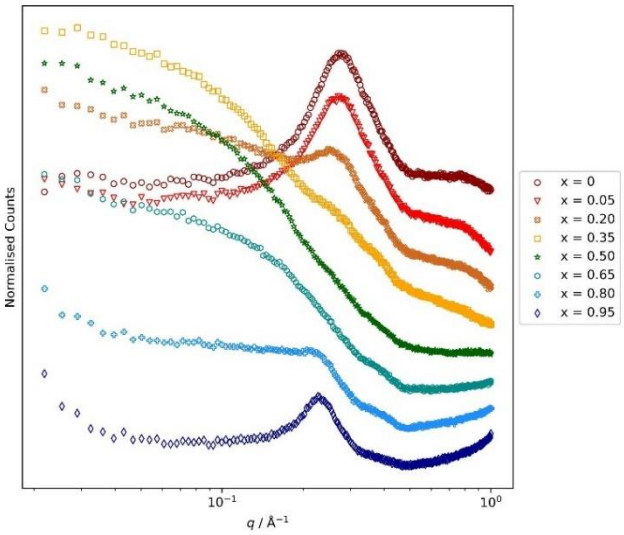

Figure S41: SANS measurements for all measurable compositions of $[C_{10}MIM]_{1-x}[C_{10}MIM\text{-}F_{17}]_x[Tf_2N]$ at 20 °C

Contrast effects on scattering

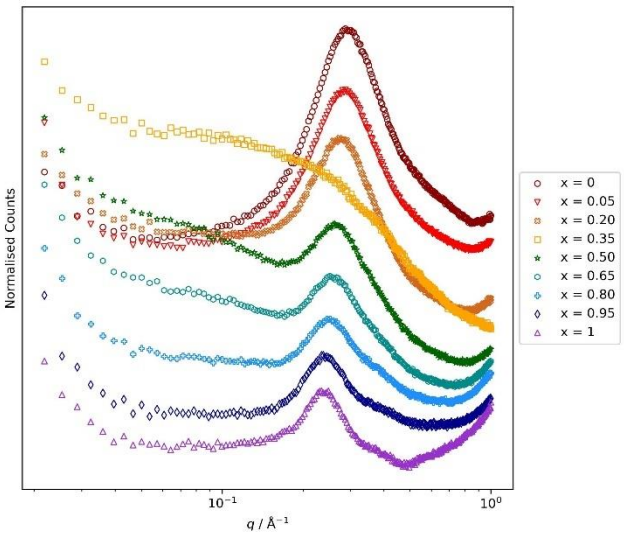

Figure S42: SANS data for $[d_{21}\text{-}C_{10}MIM]_{1-x}[C_{10}MIM\text{-}F_{17}]_x[Tf_2N]$ at 60 °C

The majority of the data in figure S41 can be fitted using the same parameters used for the non-deuterated equivalents. The samples were *x*=0.35, 0.5 and 0.65 requires a different spherical radius to be applied to achieve a good fit.

Table S5: Spherical radii required to achieve a good fit to the two contrasts measured at the compositions where different radii are required.

Composition, *x*	Spherical radius	
	h-C_{10}MIM	d_{21}-C_{10}MIM
0.35	12.0	4.6
0.50	10.8	14.1
0.65	7.8	14.7

Molecular Dynamics Simulations

All molecular dynamics simulations were conducted using DL_POLY 2.20 and GROMACS 2020 packages[6-11] at 333 K. The mixtures $[C_8MIM]_{1-x}[C_{10}MIM\text{-}F_{17}]_x[Tf_2N]$, $[C_{10}MIM]_{1-x}[C_8MIM\text{-}F_{13}]_x[Tf_2N]$ and $[C_{10}MIM]_{1-x}[C_{10}MIM\text{-}F_{17}]_x[Tf_2N]$ (x = 0, 35, 50, 85 and 100 mol%) were modelled employing the OPLS/AMBER-like CL&P force field.[12,13] The scaling factor of α = 0.8 was applied to the partial charges of the charged part of the cation and the anion. The simulations began with low-density configurations with 3500 ion pairs built with fftool and Packmol software.[14,15] The detailed simulation protocol was described in a previous work.[2] The final volumes of the simulation boxes exceeded 13 x 13 x 13 nm^3 in all cases. Pair correlation functions, $g_{ij}(r)$, and total structure factor functions, $S(q)$, were calculated following the formulas and methodologies described previously.[2]

Table S6. Position (q-Values, $Å^{-1}$, and Spacings, Å) of the Gaussian Curves Used in the Deconvolution of the MD $S(q)$ Functions. The shaded rows provide the data when a fourth Gaussian curve was used to fit the PNPP.

$[C_8MIM]_{1-x}[C_{10}MIM\text{-}F_{17}]_x[Tf_2N]$				
x	**PNPP/$Å^{-1}$ (Å)**	**PNPP2/$Å^{-1}$ (Å)**	**COP/$Å^{-1}$ (Å)**	**CP/$Å^{-1}$ (Å)**
0.00	0.354 (17.73)		0.832 (7.55)	1.372 (4.58)
0.35	0.185 (33.95)		0.839 (7.49)	1.286 (4.89)
0.50	0.220 (28.59)		0.845 (7.43)	1.259 (4.99)
0.85	0.235 (26.76)		0.855 (7.35)	1.211 (5.19)
1.00	0.230 (27.30)		0.858 (7.32)	1.193 (5.27)
0.35	0.175 (35.90)	0.186 (33.84)	0.839 (7.49)	1.286 (4.89)
0.50	0.184 (34.16)	0.232 (27.04)	0.839 (7.48)	1.254 (5.01)
0.85	0.230 (27.32)	0.235 (26.78)	0.846 (7.42)	1.208 (5.20)

$[C_{10}MIM]_{1-x}[C_8MIM\text{-}F_{13}]_x[Tf_2N]$				
x	**PNPP/Å^{-1} (Å)**	**PNPP2/Å^{-1} (Å)**	**COP/Å^{-1} (Å)**	**CP/Å^{-1} (Å)**
0.00	0.295 (21.32)		0.832 (7.55)	1.367 (4.60)
0.35	0.252 (24.96)		0.839 (7.49)	1.317 (4.77)
0.50	0.246 (25.55)		0.843 (7.45)	1.292 (4.86)
0.85	0.267 (23.51)		0.856 (7.34)	1.242 (5.06)
1.00	0.278 (22.63)		0.860 (7.31)	1.226 (5.13)
0.35	0.210 (29.90)	0.252 (24.92)	0.839 (7.49)	1.317 (4.77)
0.50	0.174 (36.01)	0.301 (20.90)	0.842 (7.47)	1.284 (4.89)
0.85	0.230 (27.37)	0.275 (22.89)	0.849 (7.40)	1.237 (5.08)
$[C_{10}MIM]_{1-x}[C_{10}MIM\text{-}F_{17}]_x[Tf_2N]$				
x	**PNPP/Å^{-1} (Å)**	**PNPP2/Å^{-1} (Å)**	**COP/Å^{-1} (Å)**	**CP/Å^{-1} (Å)**
0.00	0.295 (21.32)		0.832 (7.55)	1.367 (4.60)
0.35	0.228 (27.53)		0.843 (7.45)	1.343 (4.68)
0.50	0.222 (28.26)		0.847 (7.42)	1.265 (4.97)
0.85	0.263 (23.86)		0.859 (7.32)	1.261 (4.98)
1.00	0.230 (27.30)		0.858 (7.32)	1.193 (5.27)
0.35	0.223 (28.23)	0.274 (22.96)	0.842 (7.46)	1.340 (4.69)
0.50	0.205 (30.60)	0.227 (27.73)	0.842 (7.46)	1.262 (4.98)
0.85	0.243 (25.85)	0.272 (23.14)	0.853 (7.37)	1.259 (4.99)
$[C_8MIM]_{1-x}[C_8MIM\text{-}F_{13}]_x[Tf_2N]$				
x	**PNPP/Å^{-1} (Å)**	**PNPP2/Å^{-1} (Å)**	**COP/Å^{-1} (Å)**	**CP/Å^{-1} (Å)**
0.00	0.363 (17.31)		0.842 (7.46)	1.405 (4.47)
0.35	0.304 (20.67)		0.856 (7.34)	1.348 (4.66)
0.50	0.275 (22.85)		0.857 (7.3)	1.320 (4.76)
0.80	0.294 (21.37)		0.866 (7.26)	1.284 (4.89)
1.00	0.299 (21.01)		0.869 (7.23)	1.262 (4.98)

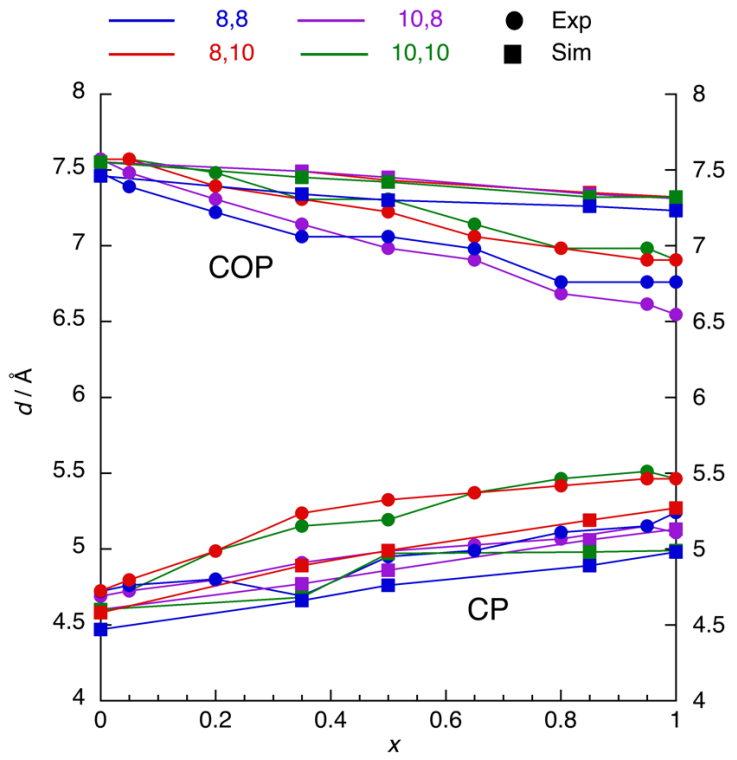

Figure S43: Comparison of the structural parameters for the CP and the COP obtained from experiment (●) and from MD simulations (■) for the mixtures: $[C_8MIM]_{1-x}[C_8MIM\text{-}F_{17}]_x[Tf_2N]$ – 8,8; $[C_8MIM]_{1-x}[C_{10}MIM\text{-}F_{13}]_x[Tf_2N]$ – 8,10; $[C_{10}MIM]_{1-x}[C_8MIM\text{-}F_{17}]_x[Tf_2N]$ – 10,8; $[C_{10}MIM]_{1-x}[C_{10}MIM\text{-}F_{13}]_x[Tf_2N]$.

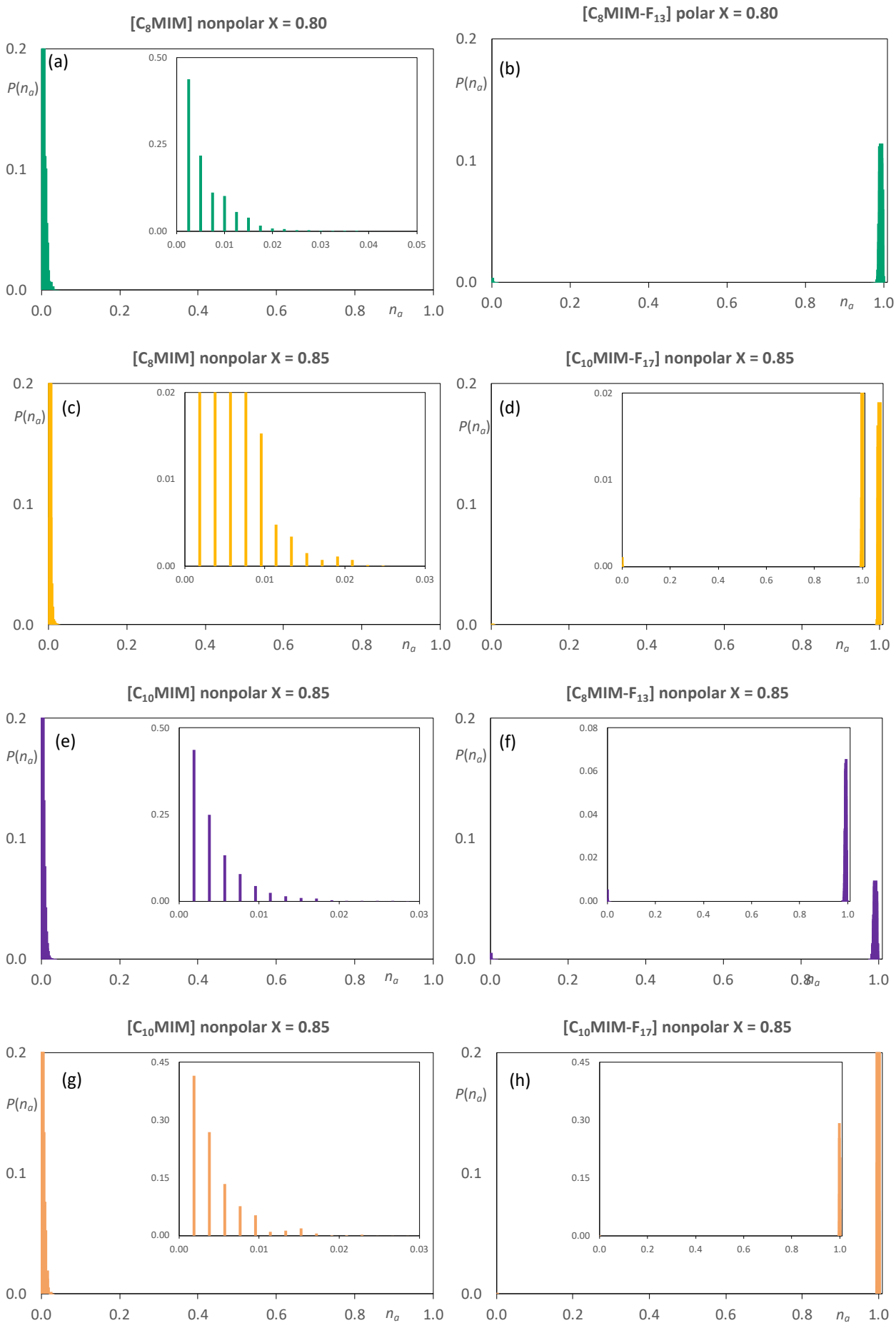
[C8MIM] nonpolar X = 0.80
(a)
P(na)
na
[C8MIM-F13] polar X = 0.80
(b)
[C8MIM] nonpolar X = 0.85
(c)
[C10MIM-F17] nonpolar X = 0.85
(d)
[C10MIM] nonpolar X = 0.85
(e)
[C8MIM-F13] nonpolar X = 0.85
(f)
[C10MIM] nonpolar X = 0.85
(g)
[C10MIM-F17] nonpolar X = 0.85
(h)

Figure S44: Discrete probability distribution function, $P(n_a)$, of the terminal chains for the different mixtures at the composition for which x = 0.85: a) hydrocarbon and b) fluorocarbon for $[C_8MIM]_{0.15}[C_8MIM\text{-}F_{13}]_{0.85}[Tf_2N]$ at 300 K; c) hydrocarbon and d) fluorocarbon for $[C_8MIM]_{0.15}[C_{10}MIM\text{-}F_{17}]_{0.85}[Tf_2N]$; e) hydrocarbon and f) fluorocarbon for $[C_{10}MIM]_{0.15}[C_8MIM\text{-}F_{13}]_{0.85}[Tf_2N]$; g) hydrocarbon and h) fluorocarbon for $[C_{10}MIM]_{0.15}[C_{10}MIM\text{-}F_{17}]_{0.85}[Tf_2N]$. Data for c)-h) at 330 K. Note that the aggregate size n_a is normalised by the total number of corresponding monomers in the MD simulation box.

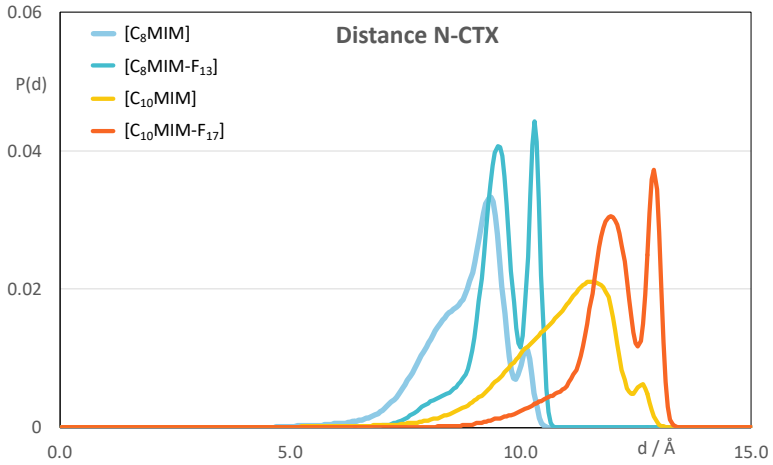

Figure S45: Probability distribution functions, $P(d)$, of the intra- molecular distances between the N atom of the imidazolium ring and the terminal carbon atoms of the alkyl chain in $[C_8MIM][Tf_2N]$ (blue line), $[C_8MIM\text{-}F_{13}][Tf_2N]$ (dark blue line), $[C_{10}MIM][Tf_2N]$ (yellow line) and $[C_{10}MIM\text{-}F_{17}][Tf_2N]$ (orange line).

1. References

1. E. J. Smoll Jr., M. A. Tesa-Serrate, S. M. Purcell, L. D'Andrea, D. W. Bruce, J. M. Slattery, M. L. Costen, T. K. Minton and K. G. McKendrick, *Farad. Discuss.*, 2018, **206**, 497–522.
2. N. S. Elstone, K. Shimizu, E. V. Shaw, P. D. Lane, L. D'Andrea, B. Demé, N. Mahmoudi, S. E. Rogers, S. Youngs, M. L. Costen, K. G. McKendrick, J. N. Canongia Lopes, D. W. Bruce and J. M. Slattery, *J. Phys. Chem. B*, 2023, **127**, 7394-7407.
3. J.-C. Buffet, V. Cristiglio, S. Cuccaro, B. Demé, B. Guérard, J. Marchal, J. Pentenero, N. Sartor and J. Turi, *EPJ Web of Conferences*, 2023, **286**, 03010. **286**, 03010.
4. MANTID: O. Arnold *et al.*, *Nucl. Instruments Methods Phys. Res. Sect. A Accel. Spectrometers, Detect. Assoc. Equip.*, 2014, **764**, 156–166.
5. M. Doucet, P. Butler, A. J. Jackson, S. King, P. Kienzle, P. Parker, J. Kryzywon, T. Richter, M. Gonzales and T. Nielsen, SASView Version 4.1.2. **2017**, https://www.sasview.org (accessed 04/03/2024).
6. W. Smith and T. R. Forester, The DL_POLY Package of Molecular Simulation Routines, (2006).
7. H. Bekker, H. Berendsen, E. Dijkstra, S. Achterop, R. Van Drunen, D. Van der Spoel, A. Sijbers, H. Keegstra, B. Reitsma and M. Renardus, *GROMACS: A Parallel Computer for Molecular Dynamics Simulations*, in: Proc. 4th Int. Conf. Phys. Comput., 1993: pp. 252–256.

8. H. Berendsen, D. Van der Spoel and R. Van Drunen, *Comput. Phys. Commun.,* 1995, **91** 43–56.
9. D. Van Der Spoel, E. Lindahl, B. Hess, G. Groenhof, A. E. Mark and H. J. C. Berendsen, *J. Comput. Chem.*, 2005, **26**, 1701–1718.
10. S. Páll, M. J. Abraham, C. Kutzner, B. Hess and E. Lindahl, *Tackling Exascale Software Challenges in Molecular Dynamics Simulations with GROMACS*, in: *Proc. EASC 2015 LNCS*, 2015: pp. 3–27.
11. M. J. Abraham, T. Murtola, R. Schulz, S. Páll, J. C. Smith, B. Hess and E. Lindahl, *SoftwareX.*, 2015, **1–2**, 19–25.
12. W. L. Jorgensen, D. S. Maxwell and J. Tirado-Rives, *J. Am. Chem. Soc.*, 1996, **118**, 11225–11236.
13. J. N. Canongia Lopes and A. A. H. Pádua, *Theor. Chem. Acc.*, 2012, **131**, 1129.
14. L. Martínez, R. Andrade, E. G. Birgin and J. M. Martínez, *J. Comput. Chem. 2*, 2009, **30**, 2157–2164.
15. A. Padua, K. Goloviznina, Z. Gong, agiliopadua/fftool: XML force field files (v1.2.1). Zenodo. https://doi.org/10.5281/zenodo.4701065, 2021. Accessed 04/03/2024.